Measure of the spatial size for the monopole excitation in proton scattering

M. Tomita,[1] M. Iwasaki,[1] R. Otani,[1] and M. Ito[1,2]
[1]*Department of Pure and Applied Physics, Kansai University, Yamatecho, 3-3-35, Suita, Osaka 564-8680, Japan*
[2]*Research Center for Nuclear Physics (RCNP), 10-1 Mihogaoka, Ibaraki, Osaka 567-0047, Japan*
(Received 17 October 2013; revised manuscript received 17 January 2014; published 21 March 2014)

We formulate a scattering radius, which will be demonstrated to be a good measure of the spatial size of a general exclusive reaction. The scattering radius is presented in a framework of the partial-wave expansion method in a general two-body scattering problem. A microscopic coupled-channel calculation is performed for proton scattering by ^{12}C in the range of the proton's incident energy, $E_p = 29.95$–200 MeV, and the scattering radii are evaluated for elastic scattering and inelastic scattering, going to the Hoyle 0_2^+ state with a well-developed 3α structure. A prominent enhancement of the scattering radius is clearly confirmed in the 3α final channel in comparison to the elastic channel. The scattering radius is also calculated for excitation to the giant monopole resonance (GMR) in a microscopic coupled-channel framework. The scattering radius for the 3α excitation is much more enhanced than the scattering radius for the GMR excitation. The proton's incident-energy dependence of the scattering radius is also investigated, and the energy systematics strongly suggest that the scattering radius can characterize the spatial size of a reaction area, which is determined by the matter radius of a nucleus excited to a final state.

DOI: 10.1103/PhysRevC.89.034619 PACS number(s): 21.60.Gx, 24.10.Eq, 25.60.Je

I. INTRODUCTION

Clustering phenomena, in which a nucleus is decomposed into subunits, is well known to appear in the excited states of a lighter mass system [1]. An α particle has a large binding energy; hence, this particle becomes a subunit or building block to construct the ground state and excited states. In ^{12}C, for instance, three α particles strongly overlap each other in the ground 0_1^+ state, while they are weakly coupled in the excited 0_2^+ state, called the Hoyle state, at $E_x = 7.65$ MeV [2–5]. In recent theoretical developments, the Hoyle state in ^{12}C is reinterpreted analogously to the Bose-Einstein condensation of the Bose α particle [4,5]. Similar α cluster structures have been established in excited 0^+ states in other systems, such as in $^{16}\mathrm{O} = \alpha + {}^{12}\mathrm{C}$ [6], $^{20}\mathrm{Ne} = \alpha + {}^{16}\mathrm{O}$ [7], etc. Excitation energies involving the cluster excitations are systematically small, below 10 MeV. Saturation in a binding energy and a matter density are the basic properties in a nucleus. Thus, a nucleus can easily break up into subunits by providing a low excitation energy. This is the main reason why a cluster structure can be realized at the low-excitation energy region.

Dilute density is a characteristic feature, commonly expected in cluster states, resulting in a large matter radius. In typical cluster systems, such as ^{12}C, ^{16}O, and ^{20}Ne, for example, all theoretical calculations predict that cluster states have about 40%–50% enhancement of a matter radius in comparison to the radius of the ground state. This spatial extension exists because a cluster state is realized at the excitation energy quite close to the threshold energy corresponding to the breakup into subunits. The formation of a cluster structure around the respective threshold energy is known as Ikeda's threshold rule [8]. In a cluster state around the threshold energy, a large part of the total binding energy is almost consumed in forming the subunits, and decomposed subunits are weakly coupled to each other. This weak-coupling feature leads to a dilute and spatially extended density distribution.

Unfortunately, the size of a cluster state is difficult to measure directly by experiments because a cluster state has a very short lifetime in general. However, much theoretical effort has been applied to searching for evidence of the spatial extension of a cluster structure in inelastic scattering, in which a target nucleus is excited to a cluster state by a projectile scattering. In inelastic scattering going to a cluster state, the range of nuclear interactions in the final cluster channel is expected to be much more extended than that in the initial channel because of the spatially extended structure of the cluster state. Specifically, the nuclear interaction is more attractive at a surface region in the final cluster channel. Such a long-range property of the nuclear interaction may be indirectly reflected in the angular distribution of the inelastic scattering. The signatures of the cluster excitation in inelastic scattering have been studied, especially in the 3α Hoyle state in ^{12}C [9–14]. There are two kinds of theoretical approaches to evidence that suggests an extended radius of the Hoyle state. One approach is analysis using a diffraction model [9–11], and the other is the coupled-channel calculation [12–14].

In the approach based on the diffraction model [9–11], the diffraction radii are estimated for the observed angular distributions according to Blair's phase rule [15]. The diffraction radius for inelastic scattering to the 0_2^+ state, which is basically determined from the peak or valley positions in the observed angular distributions, is found to be larger than that of the elastic scattering, going to the ground 0_1^+ state. From the enhanced diffraction radius, the matter radius of 0_2^+ is also speculated under a simple assumption [9]. In Ref. [11], a revised Blair's phase rule has been applied, and a similar enhancement of the diffraction radius for the 0_2^+ state has been confirmed. In these studies, an explicit value of an enhanced diffraction radius for the 3α channel is clearly obtained from the experimental data, but the origin of its enhancement still remains unclear. This is because no clear relation has been

established between the diffraction radius and an internal wave function (or a density distribution) of the 0_2^+ state.

On the contrary, in the coupled-channel approaches [12–14], nuclear interactions for the system of the ^{12}C target plus various projectiles are constructed from the folding model, which employs the internal wave function of ^{12}C, obtained from the 3α resonating group method (3α RGM) [2] and from an effective density-dependent nucleon-nucleon interaction. This coupled-channel calculation is called microscopic coupled-channels (MCC) [16]. Because the 3α RGM wave function can precisely describe the 3α structure in 0_2^+, the constructed nuclear interaction in the 0_2^+ channel is more attractive at a surface region than the interaction in the ground channel. The MCC calculations employing the folding interaction have been applied to the $\alpha + {}^{12}$C [12] and ^{3}He $+ {}^{12}$C [13,14] systems, and the calculation nicely reproduces the angular distributions of various exit channels. In the differential cross section for the 0_2^+ channel, a scattering angle for the first Airy minimum is shifted to the larger angle region, and the number of the Airy minima increases in a comparison to other inelastic channels, going to the rotational and vibrational states such as the 2_1^+ and 3_1^- states. From this result, the authors have claimed that the evolution of the Airy structure originated from the spatial extension of the nuclear interaction in the final 0_2^+ channel [12–14].

In the nuclear reaction, the final 3α states can be assessed through the transition from the incident ground channel, and the 3α state is observed as the final state in the reaction process. Therefore, a coupling potential, which induces a transition from the initial channel to the final channel, is expected as a main ingredient for the angular distribution of the inelastic scattering, and the distortion potential or the density distribution in the exit channel may provide a minor contribution. In fact, a dominance of the coupling potential in the inelastic scattering has been pointed out by Takashina *et al.* [17,18]. By employing the MCC calculation, which is the same method as in Refs. [12–14], the authors have clearly demonstrated that the Airy structure in the angular distribution is dominated not by the size of the 0_2^+ state, but by a spatial distribution of the coupling potential for the $0_1^+ \rightarrow 0_2^+$ transition.

Although the potential or density distribution in the final 3α channel itself plays a minor role in inelastic scattering, a coupling potential contains size information of the final 3α state because the coupling potential is determined by an overlap of the wave function between the initial ground state and the final 3α state. Therefore, an extended structure of the 3α state is indirectly reflected in the inelastic scattering to the 3α final state. Thus, it is still useful to consider a relation between an inelastic scattering and the internal size of the 3α structure. To discuss the relation of the spatial size of the 3α state and inelastic scattering clearly, a "radius" of the inelastic scattering should be clearly defined in the MCC framework, as has been done in the approach of the diffraction model [9–11].

In the present paper, we propose a "scattering radius," which characterizes the spatial size of exclusive reactions. The scattering radius is simply defined from the partial cross sections, which can be obtained from the partial-wave decomposition of the Schrödinger equation. Therefore, the scattering radius defined in this article can always be determined in a standard scattering problem using partial-wave expansion. The scattering radius does not necessarily represent the matter radius of the finally excited state, but it characterizes a size of the spatial area, where a scattering or a transition occurs. The scattering radius can be used to measure the size of various reaction channels; hence, its enhancement can be clearly discussed in connection with the internal structure of a final state.

First, we perform the MCC calculation for $p + {}^{12}$C, which is similar to the calculation shown in Refs. [12–14,16–18]. Second, we compare the differential cross sections with the theoretical calculation. Third, the scattering radius is derived from the partial cross sections, and we demonstrate that the scattering radius for the 0_2^+ channel is much more enhanced than that for the ground 0_1^+ channel. Furthermore, we also assume a monopole compression mode at the excitation energy of 35 MeV, which simulates the giant monopole resonance (GMR) in ^{12}C [19]. The MCC calculation is performed for the inelastic scattering going to the GMR state, and the scattering radius for the GMR excitation is compared with the scattering radius for the 3α state. A prominent difference arises in the scattering radius of these two excitation modes because of a large difference in the excitation energy between the 3α state (7.65 MeV) and the GMR state (35 MeV).

The organization of this article is as follows. In Sec. II, the definition of the scattering radius and the framework of the MCCs are explained. In Sec. III, the theoretical calculation for $p + {}^{12}\mathrm{C}_{\mathrm{g.s.}}$ elastic scattering and inelastic scattering to $p + {}^{12}\mathrm{C}(0_2^+)$ are compared with the experiments. The partial-wave analysis is performed for the theoretical cross section, and the scattering radii for the ground and 3α channels are derived. In Sec. IV, an inelastic scattering to GMR is performed, and the scattering radius for the GMR excitation is compared with the 3α excitation. The incident-energy dependence of the scattering radius is discussed in Sec. V. The final section is devoted to a summary of the findings and a discussion.

II. FRAMEWORK

A. Definition of the scattering radius

We consider a simple scattering system, a nucleon plus a spinless target. In this case, a Schrödinger equation for a nucleon scattering system is expanded in terms of the total spin J and the orbital spin L for nucleon-target relative motion. Thus, the resultant partial cross sections σ are labeled by J, L, and an internal energy of a target ϵ; hence, $\sigma \equiv \sigma(JL\epsilon)$. Here the partial cross sections represent the scattering probability generated by a nuclear interaction, and the Coulomb scattering part is excluded. The nuclear part of the partial cross sections, $\sigma(JL\epsilon)$, can be calculated for all the exit subchannels specified by L and ϵ at a fixed J.

From the partial cross section, we define an effective orbital spin $\bar{L}$ as

$$\bar{L}_{\mathrm{I}}(\epsilon) = \sqrt{\frac{\sum_{JL} \tilde{L}^4 \sigma(JL\epsilon)}{\sum_{JL} \tilde{L}^2 \sigma(JL\epsilon)}}, \tag{1}$$

with a definition of $\tilde{L} = \sqrt{L(L+1)}$. The effective orbital spin is obtained by the ratio of the fourth and second moments of the magnitude of the orbital spin, $\sqrt{L(L+1)}$. We assume Eq. (1) in an analogy to the usual matter radius. A matter radius $\bar{r}$ (root-mean-squared radius) is usually calculated from the matter density in the ground state, $\rho_{0_1^+}(r)$, such that

$$\bar{r} = \sqrt{\frac{\int dr r^4 \rho_{0_1^+}(r)}{\int dr r^2 \rho_{0_1^+}(r)}}. \tag{2}$$

The matter radius $\bar{r}$ is obtained by the ratio of the r^4 moment and the r^2 moment for the ground-state density. Thus, Eq. (1) is obtained by simply replacing $r \to \tilde{L}$ and $\rho_{0_1^+}(r) \to \sigma(JL\epsilon)$ in Eq. (2). $\bar{L}(\epsilon)$ is a representative value of an incident orbital spin, which mainly contributes to the reaction going to an exit channel with a target internal energy of ϵ. We call the definition of Eq. (1) measure (I) of an effective orbital spin, which is shown by the subscript of I in Eq. (1).

A factor of r^2 contained in both the numerator and the denominator in Eq. (2) originates from the volume element in the spherical coordinate system. Thus, this element would be excluded in the definition of $\bar{L}$, and the resultant definition should be modified to

$$\bar{L}_{\rm II}(\epsilon) = \sqrt{\frac{\sum_{JL} \tilde{L}^2 \sigma(JL\epsilon)}{\sum_{JL} \sigma(JL\epsilon)}}. \tag{3}$$

We call this definition measure (II). Other definitions will also be available for $\bar{L}$, but in the present analysis, we consider only these two kinds of an effective orbital spin. The possibility of another type of $\bar{L}$ will be investigated in future studies.

Once the effective orbital spin $\bar{L}$ is determined, we can characterize the spatial size of the scattering area. Here we introduce the scattering radius $R_{\rm SC}$ from $\bar{L}$ and incident wave number k as

$$\bar{L}(\epsilon) = k R_{\rm SC} \to R_{\rm SC} = \frac{\bar{L}(\epsilon)}{k}, \tag{4}$$

where the wave number k is measured in a laboratory system. This relation is just a simple classical relation between an incident orbital spin $\bar{L}$ and a radius of $R_{\rm SC}$, corresponding to an impact parameter. Because $\bar{L}(\epsilon)$ represents the effective orbital spin of the incident wave scattered to a final channel with a label of ϵ, the scattering radius in Eq. (4) corresponds to the size of the spatial area, where a specific reaction occurs. Therefore, the scattering radius can characterize the radius of an exclusive reaction in contrast to a radius for an inclusive reaction derived for deuteron-induced reactions [20].

In the present formulation of the scattering radius, we have restricted a system to a nucleon scattering by a spinless target, but the definition of the scattering radius can be easily extended to general two-body scattering systems, which contains a target spin, rearrangement channels, and so on. Furthermore, the partial cross sections are always defined in a standard scattering calculation, which employs the partial-wave-expansion method. Therefore, the calculation of the scattering radius is available in a general scattering calculation similar to the method of coupled-channels and the distorted-wave Born approximation.

B. High-energy limit of the scattering radius in a black sphere model

Let us discuss a quantitative feature of the effective orbital spin, given by Eqs. (1) and (3), and the respective scattering radii in the case of a simple potential scattering of a point particle. Here we consider the limit of the high-energy scattering by a black sphere potential with a radius of $R_{\rm BS}$. The black sphere is assumed to have a uniform distribution with a sharp edge; hence, the maximum orbital spin $L_{\rm max}$, which can contribute to the scattering cross section, is exactly determined by the relation of $L_{\rm max} = k R_{\rm BS}$ with an incident momentum k. All the partial waves below $L_{\rm max}$ are completely absorbed, and a scattering matrix S_L with the partial wave L satisfies $S_L = 0$ for $L \leqslant L_{\rm max}$. In this situation, the partial cross section $\sigma_{\rm BS}(L)$ is proportional to $2L+1$.

The explicit value of the effective orbital spin can be calculated for the scattering by the black sphere. For simplicity, $\tilde{L}$ is replaced by L in Eqs. (1) and (3). By substituting $\sigma_{\rm BS}(L) \propto 2L+1$ in Eqs. (1) and (3), the summation over $L = 0 \sim L_{\rm max}$ can be explicitly evaluated. If we take the high-energy limit of $k \to \infty$, we can obtain the relation of $R_{\rm SC}$ and $R_{\rm BS}$

$$\bar{L}_{\rm I} \sim \sqrt{\frac{2}{3}} k R_{\rm BS} \to R_{\rm SC}({\rm I}) \sim 0.82 R_{\rm BS}, \tag{5}$$

$$\bar{L}_{\rm II} \sim \sqrt{\frac{1}{2}} k R_{\rm BS} \to R_{\rm SC}({\rm II}) \sim 0.71 R_{\rm BS}. \tag{6}$$

The scattering radii derived from the effective orbital spins reach about 70%–80% value of the black sphere radius in the high-energy limit.

Furthermore, the scattering radius in Eqs. (5) and (6) can be directly connected to the matter radius of the target nucleus on the basis of pioneering work of the black sphere model by Kohama *et al.* [10]. In the black sphere model, there is a relation between the real radius of the black sphere $R_{\rm BS}$ and its root-mean-square radius $r_{\rm BS}$,

$$r_{\rm BS} = \sqrt{\frac{3}{5}} R_{\rm BS}. \tag{7}$$

According to the sophisticated analysis of the proton elastic scattering in Ref. [10], the root-mean-square radius of a target nucleus, $\bar{r}$, is almost the same as $r_{\rm BS}$. Specifically, a relation of

$$r_{\rm BS} \sim \bar{r} \tag{8}$$

has been established, at least, for the target mass $A \geqslant 50$ and $E_p \sim 800$ MeV. From the relations of Eqs. (7) and (8), we can obtain a relation between $R_{\rm SC}$ and $\bar{r}$ such that

$$R_{\rm SC}({\rm I}) = \sqrt{\frac{2}{3}} R_{\rm BS} = \sqrt{\frac{2}{3}}\sqrt{\frac{5}{3}} \bar{r} \sim 1.05 \bar{r}, \tag{9}$$

$$R_{\rm SC}({\rm II}) = \sqrt{\frac{1}{2}} R_{\rm BS} = \sqrt{\frac{1}{2}}\sqrt{\frac{5}{3}} \bar{r} \sim 0.91 \bar{r}. \tag{10}$$

These results clearly show a direct relation between the scattering radius and a root-mean-square radius of the target nucleus. In the high-energy limit of an elastic scattering by a black sphere, the scattering radius naturally gives almost the

same value as the matter radius of the target nucleus with a deviation of 5%–10%. Therefore, the black sphere evaluations of the scattering radius support the validity of the concept of the scattering radius introduced here.

In the high-energy limit of a realistic elastic scattering, $R_{\rm SC}$ should give a radius at least comparable to or considerably larger than the matter radius $\bar{r}$ of the target nucleus. This is because the elastically scattered projectile feels the nuclear potential generated by the target nucleus, which has a longer range than the range of the matter radius. This condition on the scattering radius is a moderate criterion in which either measure (I) or measure (II) is chosen.

C. Coupled-channel equations and folding potential

To calculate the partial cross section, we solve a set of the coupled-channel equation for the proton-^{12}C system, which is given in the symbolic form

$$[T_f(\mathbf{R}) + V_{f,f}(\mathbf{R}) - E_f]\chi_f(\mathbf{R}) = -\sum_{i\neq f} V_{f,i}(\mathbf{R})\chi_i(\mathbf{R}). \quad (11)$$

Here the subscripts of f and i design a channel. This coupled-channel equation is solved in a subspace of the total spin of J and the orbital spin of L, and the partial cross sections $\sigma(JL\epsilon)$ are obtained.

$T_f(\mathbf{R})$ represents the kinetic energy of the relative motion of the $p + {}^{12}$C system with a relative coordinate $\mathbf{R}$, while $V_{f,i}(\mathbf{R})$ denotes the coupling potential for the transition from channel i to channel f. The total energy in the channel f, E_f, is given by the relation of $E_f = E - \epsilon_f$ with the proton's incident energy E and the target internal energy of ϵ_f. $\chi_f(\mathbf{R})$ is the proton-^{12}C relative wave function for the channel f, which should be solved in the coupled-channel equation. In the present calculation, we restrict the computational channels to the incident and exit channels to pin down the essential feature of the scattering radius. Thus, the subscripts f and i represent either the ground 0^+_1 channel or the Hoyle 0^+_2 channel.

There are also possible transitions beyond the two-channel calculation, such as $0^+_1 \to 2^+_1(\text{or } 3^-_1) \to 0^+_2$, which passes through the collective 2^+_1 (or the 3^-_1) state. However, such two-step transitions have been found to play minor roles in the $\alpha + {}^{12}$C scattering at $E/A = 43$ and 60 MeV [17,18]. In the proton plus ^{12}C scattering going to the Hoyle 0^+_2 state, therefore, a major transition process is expected to be at least a direct excitation of $0^+_1 \to 0^+_2$ in the energy region of $E_p \geqslant 40$ MeV. Thus, the two-channel calculation of 0^+_1 and 0^+_2 can cover the essential feature of the inelastic scattering to the 0^+_2 state. In fact, we have also performed the coupled-channel calculation including the 2^+_1 and the 3^-_1 states, but the coupling effect of 2^+_1 and 3^-_1 just changes the magnitude of the differential cross section in the two-channel calculation by about 20% at a maximum. The oscillating pattern of the two-channel calculation is almost unchanged even if the 2^+_1 and the 3^-_1 states are coupled.

The real part of the diagonal ($f = i$) and coupling potentials ($f \neq i$), $V_{f,i}(\mathbf{R})$, is calculated by the folding model [16,21], which is expressed symbolically as

$$V_{f,i}(\mathbf{R}) = N_R \int \rho_{f,i}(\mathbf{r}) v_{NN}(\mathbf{r} - \mathbf{R})\, d\mathbf{r}, \quad (12)$$

where $\mathbf{r}$ denotes the coordinate measured from the center of the mass in the ^{12}C nucleus. Here $\rho_{f,i}(\mathbf{r})$ represents the diagonal ($f = i$) or transition ($f \neq i$) densities of ^{12}C, which are calculated by the microscopic 3α cluster model, resonating group method (RGM) [2]. In general reaction calculations, a normalization constant N_R is introduced because the folding potential contains a theoretical ambiguity in its strength.

In Eq. (12), v_{NN} represents the effective nucleon-nucleon (NN) interaction which acts between a nucleon contained in ^{12}C and an incident proton. In the present calculation, we adopt the M3Y (Michigan 3-range Yukawa) interaction [22]. The central part of the coupling potentials, $V^{\rm CE}_{f,i}(R)$, are calculated by folding the central part of M3Y, which is given by

$$v^{\rm M3Y}_{NN}(s) = 7999\frac{e^{-4s}}{4s} - 2134\frac{e^{-2.5s}}{2.5s} - J_0\delta(\mathbf{s}). \quad (13)$$

In the central part, there is no contribution from the long-range attractive potential generated by the one-pion exchanges. The third term simulates the single nucleon's knock-on exchange with the strength of $J_0 = -262$ MeV fm^3 [21].

In addition to the central potential, we introduce the spin-orbit interaction. If we adopt the short-range property of the NN spin-orbit potential, the folded spin-orbit potential for a nucleon-nucleus system has the following simple form [23]:

$$V^{\rm LS}_{f,i}(R) = U^{\rm LS}_{f,i}(R)\mathbf{L}\cdot\sigma, \quad (14)$$

$$U^{\rm LS}_{f,i}(R) = -\frac{\pi}{2}\frac{1}{R}\frac{\partial\rho_{f,i}(R)}{\partial R}\int v^{\rm M3Y}_{\rm TO}(s)s^4 ds. \quad (15)$$

Here $\rho_{f,i}(R)$ denotes the monopole (spherical) transition density, while $\mathbf{L}$ and σ denote the vectors of the orbital spin and Pauli's spin matrices, respectively. In Eq. (15), $v^{\rm M3Y}_{\rm TO}$ represents the triplet-odd part of the M3Y spin-orbit interaction, and its explicit form is

$$v^{\rm M3Y}_{\rm TO}(s) = -3733\frac{e^{-4s}}{4s} - 427.3\frac{e^{-2.5s}}{2.5s}. \quad (16)$$

This effective spin-orbit potential is obtained from the Reid NN potential [22]. In the derivation of Eq. (15), the cancellation of the triplet-even part and knock-on exchange is assumed [23].

The M3Y interaction is a density-independent g matrix calculated in infinite nuclear matter at a fixed nucleon density [22]. In modern studies of nuclear reactions, density-dependent g matrices, such as the density-dependent version of M3Y [24,25], the Melbourne interaction [26], and complex effective Gaussian form factor [27], are often employed in calculations of folding potentials. The density-dependent g matrix seems to be more sophisticated than the density-independent interaction, M3Y. However, nuclear potentials generated from a density-dependent force still need a considerable normalization factor to reproduce the experimental data [12–14]. Thus, a density-dependent nucleon-nucleon interaction is not perfect in the present application of folding models. Furthermore, in the density-independent force, there is a great advantage in Eq. (15); the folded spin-orbit potential has a separable form of the density-derivative part and a volume-integral part of the nucleon-nucleon (triplet-odd) spin-orbit force. From Eq. (15), we can deduce a relation between the density distribution and

the spin-orbit splitting if we calculate the energy spectra with the same interactions. Because we intend to conduct future studies on spin-orbit splitting for a nucleon-nucleus system, we apply the density-independent M3Y interaction to the present scattering problem.

D. Phenomenological complex potential

Because the M3Y NN interaction is real, the resultant folding potential only includes a real part. In the usual treatment of scattering phenomena, imaginary potentials are introduced, and their parameters are optimized so as to reproduce the experimental observables. Generally speaking, the imaginary potential simulates a part of the dynamic polarization potential (DPP), which is a coupling with channels outside of computational model space. Here we introduce the complex potential for a diagonal transition in the incident and exit channels to take into account the DPP effect. Because the nuclear structures of ^{12}C are very different between the incident 0_1^+ channel (spatially compact structure) and the exit 0_2^+ channel (well-developed 3α structure), the strong channel dependence of DPP is expected. The parameters of the complex potentials are basically searched to reproduce the experimental data, but the obtained parameters are tuned to simulate the qualitative features expected from the internal structure of the ^{12}C nucleus.

In the elastic channel, we add the central imaginary potential $-iW(R)$ to the M3Y folding potential such that

$$V_{i,i}(R) = V_{i,i}^{\rm CE}(R) + V_{i,i}^{\rm LS}(R) - iW_i(R), \quad (17)$$

$$W_i(R) = W_V(R) + W_S(R), \quad (18)$$

with $i =$ elastic channel ($p + {}^{12}{\rm C}_{\rm g.s.}$). Here $W_i(R)$ is given by the summation of the Woods-Saxon (WS) potential with volume-type $W_V(R)$ and surface-type $W_S(R)$ form factors. The subscripts of V and S denote the volume-type and surface-type WS potentials, respectively. The three parameters strength (W_0), radius (R_I), and diffuseness (a_I) are included in each of the WS potentials: (W_{0V}, R_{IV}, a_{IV}) in $W_V(R)$ and (W_{0S}, R_{IS}, a_{IS}) in $W_S(R)$.

In the exit 0_2^+ channel, we do not consider a simple absorptive potential, but the complex potential,

$$V_{f,f}(R) = V_{f,f}^{\rm CE}(R) + V_{f,f}^{\rm LS}(R) + V_{f,S}(R) - iW_f(R), \quad (19)$$

with $f =$ inelastic channel ($p + {}^{12}{\rm C}(0_2^+)$). Here a form factor of $W_f(R)$ is taken to be the same form in Eq. (18). In this channel, we include the real attractive WS potential $V_{f,S}(R)$ with the surface form factor, which contains the three parameters (V_{0S}, R_S, a_S). Because the 0_2^+ state corresponds to a resonant state with a strong deformation, the excitation to its rotational unbound state, 2_2^+, strongly occurs. The $B(E2)$ value for the transition of $0_2^+ \to 2_2^+$ is 25 times stronger than that for the respective yrast transition, $0_1^+ \to 2_1^+$ [2]. Therefore, the strong excitation of $0_2^+ \to 2_2^+$ is expected in the proton scattering. If the channel coupling is extremely strong, DPP cannot be simulated by a simple attractive imaginary potential, and a strong real potential is generated in DPP [28]. Thus, we introduce the real potential in the final 3α channel owing to its strong coupling to the unbound rotational excitations.

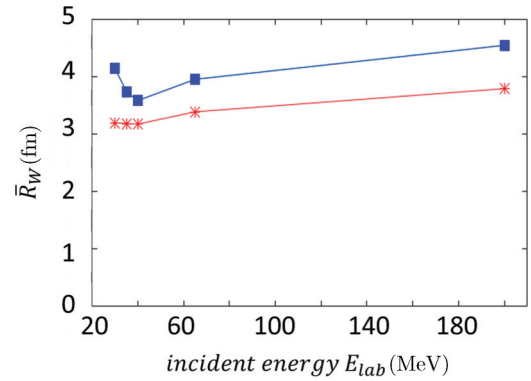

FIG. 1. (Color online) Incident-energy dependence of the mean radius of the imaginary potentials. The solid squares show the radii for the 0_2^+ channel, while the crosses are the radii for the ground 0_1^+ channel.

The parameter sets for the incident and exit 3α channels, which are determined so as to reproduce the experimental cross sections as much as possible, are listed in the Appendix (Tables IV and V). In these calculations, the normalization factor in the folding potential is set to $N_R^{\rm CE} = 1$ for the central part and $N_R^{\rm LS} = 1.1$ for the spin-orbit part. In Fig. 1, the energy dependence of the mean radius of the imaginary potential,

$$\bar{R}_W = \sqrt{\frac{\int R^2 W(R) d\mathbf{R}}{\int W(R) d\mathbf{R}}}, \quad (20)$$

are plotted.

The solid squares and the crosses represent the mean radius for the 0_2^+ channel and the ground 0_1^+ channel, respectively. Both potentials have a weak energy dependence, and the mean radius for the 0_2^+ channel is larger by about 1 fm than that for the ground channel in the whole incident-energy region. This means that the 0_2^+ channel feels a strong and long-range absorption, and this feature is consistent with the DPP analysis in the $^{12}{\rm C} + {}^{12}{\rm C}$ system at the molecular-resonance energy region [29]. The similar long-range properties of absorption in the 0_2^+ channel are also reported in the inelastic scattering of $\alpha + {}^{12}{\rm C}$ [12,13,30] and ${}^3{\rm He} + {}^{12}{\rm C}$ [14]. The strong and long-range absorption for the 0_2^+ channel originates from the weak binding property of the 0_2^+ state, which finally breaks up into continuum states. The density distribution of 0_2^+ is more extended than that of the ground state. Therefore, the absorption for the 0_2^+ channel occurs at the outer region in comparison to the ground 0_1^+ channel, and the resultant absorption potential has a long range in the 0_2^+ channel as shown in Fig. 1.

III. PARTIAL-WAVE ANALYSIS AND THE SCATTERING RADIUS

A. Calculation of the differential cross section

In this section, we compare the theoretical calculation with the experimental differential cross section. Figure 2 shows the results of the differential cross sections at $E_p = 65$ MeV. In this calculation, we keep $N_R^{\rm CE} = 1$ and $N_R^{\rm LS} = 1.1$ in the central and spin-orbit folding potentials, respectively. Panel (a) shows the comparison in the elastic scattering, while panel

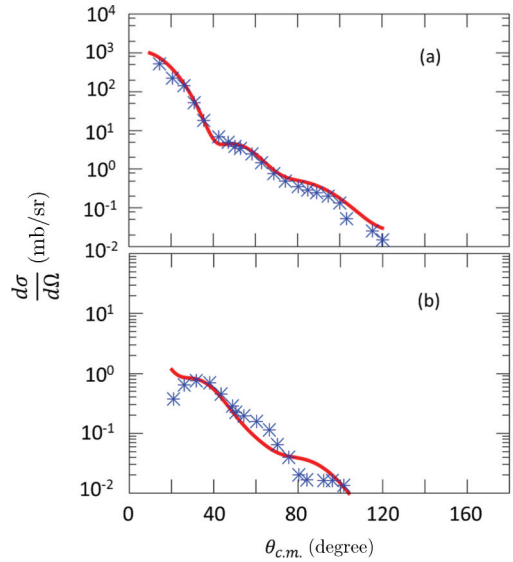

FIG. 2. (Color online) Differential cross section at $E_p = 65$ MeV. Panel (a) shows the result of the elastic (0_1^+) channel, while the result of the inelastic (0_2^+) channel is plotted in panel (b). In both panels, the asterisks and curves represent the experimental data and the theoretical calculations, respectively.

(b) displays the inelastic scattering to the 0_2^+ state. In the elastic scattering, the present MCC calculation nicely reproduces the experimental cross sections over the observed angular range. On the contrary, the calculation for the 0_2^+ channel reproduces a global tendency observed in the inelastic scattering, although the oscillation of the calculated cross section is out of phase in comparison to the experiments.

To obtain a better fit, we must vary the normalization constant N_R considerably in the folding potential. By changing the N_R and the parameters in the complex potential, we can obtain several parameter sets, which can reasonably reproduce the observed angular distributions. The existence of the several parameter sets means that an ambiguity arises in the calculation of the effective orbital spin $\bar{L}$ and the scattering radius $R_{\rm SC}$. Specifically, several $\bar{L}$ and $R_{\rm SC}$ can be obtained for the individual parameter sets. In the following sections, we discuss $\bar{L}$ and $R_{\rm SC}$ derived from the calculation with $N_R^{\rm CE} = 1$ and $N_R^{\rm LS} = 1.1$ (Fig. 2), and the ambiguity of $\bar{L}$ and $R_{\rm SC}$ is discussed in Sec. V.

B. Evaluation of the scattering radius

In the previous section, we confirmed that the MCC calculation can reasonably reproduce the scattering observables at $E_p = 65$ MeV. In this section, we show the partial-wave analysis and derive the scattering radius for both the elastic and the 0_2^+ channels at this incident energy. In Fig. 3, the partial cross sections for the elastic (asterisks) and the inelastic scattering (squares) are shown. In the elastic scattering, the nuclear part of the partial cross sections are plotted in Fig. 3. Each of the partial cross sections, $\sigma(JL\epsilon)$, has the labels of the total spin J and the orbital spin L. In Fig. 3, $\sigma(JL\epsilon)$ with an allowed L is summed up for a fixed J such that $\sigma(J\epsilon) = \sum_L \sigma(JL\epsilon)$.

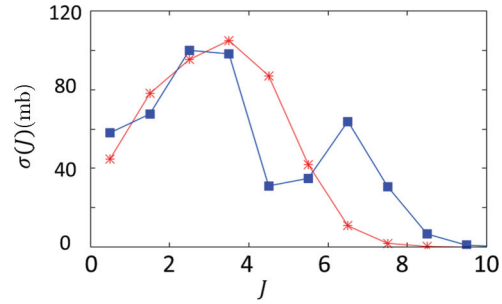

FIG. 3. (Color online) Distributions of partial cross sections at $E_p = 65$ MeV. The asterisks represent the partial cross sections $\sigma(J)$ for the elastic scattering, while the distribution with the squares shows the cross section for the inelastic scattering. The inelastic partial cross sections are multiplied by a factor of 200 to be shown in the same scale as the elastic scattering.

We can clearly confirm a prominent difference in a comparison of the elastic partial cross section with the inelastic partial cross section. The elastic partial cross section has a peak at $J = 7/2$, and its magnitude is monotonically damped at $J = 15/2$. On the contrary, double peak structures are observed in the inelastic scattering going to the 0_2^+ state. There is a strong peak at $J = 7/2$ and $J = 13/2$, and considerable magnitude continues up to $J = 19/2$. Because the scattered orbital spin has a close connection to the spatial size of a potential produced by the target, the distribution shown in Fig. 3 strongly suggests that a spatial area of scattering is prominently different in these two channels.

From the distributions of the partial cross section, we evaluate the effective orbital spin $\bar{L}$ and the scattering radius $R_{\rm SC}$ according to the definitions given in Eqs. (1), (3), and (4). The obtained values are summarized in Table I. In the top row, the $\bar{L}$ and $R_{\rm SC}$ for the elastic channel, derived from measure (I) [Eq. (1)] and measure (II) [Eq. (3)] are shown. In measure (I), $\bar{L}_I = 4.69$ and $R_{\rm SC}(\rm I) = 2.65$ fm, while $\bar{L}_{\rm II} = 3.66$ and $R_{\rm SC}(\rm II) = 2.07$ fm in measure (II). In measure (I), the elastic $R_{\rm SC}(\rm I)$ is larger by about 10% than the matter radius of the ground-state density calculated by the 3α RGM ($\bar{r} = 2.40$ fm) [2], which is comparable to the charge radius ($\bar{r}_{\rm ch} = 2.53$ fm). On the contrary, in the case of measure (II), $R_{\rm SC}(\rm II)$ for the elastic channel is smaller by about 15% than the ground matter radius.

TABLE I. Effective orbital spins $\bar{L}_{\rm I,II}$ and the scattering radius $R_{\rm SC}$(I,II) calculated from the definition in Eqs. (1), (3), and (4). The theoretical mean radius of the density distribution ($\bar{r}$) for the ground 0_1^+ ($E_x = 0.00$ MeV) and 0_2^+ ($E_x = 7.65$ MeV) states are also shown in the second column from the right. In the rightmost column, the diffraction radii obtained in Ref. [11] are shown for a comparison. $R_{\rm SC}$ and $\bar{r}$ are shown in units of fm, while the excitation energy (E_x) is shown in units of MeV.

Channel	E_x	$\bar{L}_{\rm I}$	$R_{\rm SC}$(I)	$\bar{L}_{\rm II}$	$R_{\rm SC}$(II)	$\bar{r}$	Ref. [11]
0_1^+	0.00	4.69	2.65	3.66	2.07	2.40	2.75 ± 0.06
0_2^+	7.65	6.13	3.46	4.26	2.41	3.47	3.20 ± 0.07

The results for the 3α cluster states, 0_2^+, are shown in the bottom row: $[\bar{L}_I, R_{\rm SC}({\rm I})] = (6.13, 3.46\ {\rm fm})$ for measure (I) and $[\bar{L}_{\rm II}, R_{\rm SC}({\rm II})] = (4.26, 2.41\ {\rm fm})$ for measure (II). The $R_{\rm SC}$ in measure (I) is comparable to the matter radius of the 0_2^+ state obtained in 3α RGM($\bar{r} = 3.47$ fm) [2]. In accordance with the broad structure in the inelastic partial cross section shown in Fig. 3, $R_{\rm SC}$ in the inelastic 0_2^+ channel is enhanced in comparison to that in the elastic channel. This enhancement is common feature in both measures of (I) and (II). The enhancements of the scattering radius in the 0_2^+ channel amount to ∼30% in measure (I) and ∼20% in measure (II).

Because it is reasonable that the scattering radius in the elastic channel is comparable to or considerably larger than the matter radius of the ground state, measure (I) is considered to be appropriate to characterize the size of the scattering area. In the rightmost column, the diffraction radii obtained from the proton scattering at $E_p = 1040$ MeV are shown for comparison [11]. The proton incident energies are very different between the present calculation and the analysis of the diffraction model. Nevertheless, the scattering radii obtained from measure (I) give almost the same values as the diffraction radii. Thus, in the following analysis, we use measure (I) to calculate the scattering radius, although measure (II) is not inadequate in the discussion of the scattering radius.

C. Distortion effect in the exit channel

As we have just confirmed in Table I, the scattering radius for the inelastic 0_2^+ channel is prominently enhanced in both measures (I) and (II). This enhancement strongly suggests that the spatial extension of the 3α structure is directly reflected in inelastic scattering. However, inelastic scattering corresponds to a transition from an incident channel to an exit channel, and its cross section does not necessarily directly reflect the size of a potential in an exit channel. Therefore, we need a careful analysis for the origin of this strong enhancement in the scattering radius of the inelastic 3α channel.

In this section, we discuss the main origin of the enhanced scattering radius confirmed in the inelastic scattering to the 0_2^+ state. In elastic scattering, the diagonal (distortion) potential of the incident channel mainly determines the differential cross section. Thus, the scattering radius obtained from the elastic scattering directly provides size information of the distortion potential in the incident channel. In inelastic scattering, however, there are two main ingredients which determine the scattering cross section: a coupling potential inducing the transition from an incident channel to an exit channel, and the distortion potential in an exit channel.

The effect of the distortion potential in the exit 0_2^+ channel can be seen in Fig. 4. This figure shows the distribution of the inelastic partial cross sections with and without the distortion effect in the exit channel. The solid squares show the result of the full MCC calculation, which has already been shown in Fig. 3 (squares), while the circles represent the restricted MCC calculation without the distortion potential in the exit channel. As can clearly be seen in Fig. 4, distribution of the higher partial waves is almost unchanged, but the lower partial-wave contribution increases in the restricted MCC calculation as shown by the circles.

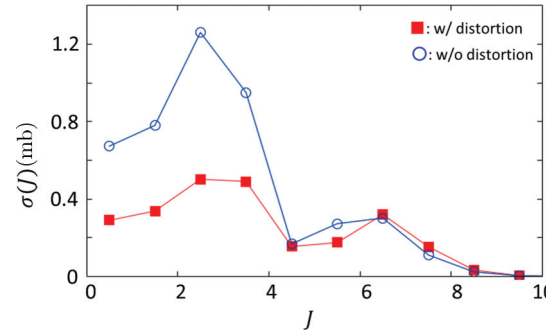

FIG. 4. (Color online) Partial cross sections for inelastic scattering at $E_p = 65$ MeV. The squares show the results of the full CC calculation, while the circles show the results without any potentials in the exit 0_2^+ channel. The distribution with the squares is the same as the distribution with the squares shown in Fig. 3.

Let us discuss the behavior of the partial cross section based on the transition amplitude of the distorted-wave Born approximation (DWBA), $T^{JL}_{\rm DWBA} = \langle \chi^{JL}_{0_2^+} | V_{\rm cp} | \chi^{JL}_{0_1^+} \rangle$, where χ^{JL}_α denotes the distorted wave for the partial wave JL in the channel α ($\alpha = 0_1^+$ or 0_2^+). The magnitude of the transition amplitude is determined by the overlap of the final distorted wave $\chi^{JL}_{0_2^+}$ and the coupling potential $V_{\rm cp}$. In Fig. 5, the central part of the diagonal folding potential ($V_{\rm dg}$) of the 0_1^+ (dashed curve), 0_2^+ (thick curve) channels and the coupling potential ($V_{\rm cp}$) of $0_1^+ \to 0_2^+$ (dotted curve) are plotted. The squares and the circles in Fig. 4 correspond to the calculations with and without the diagonal potential of the 0_2^+ channel (thick curve in Fig. 5), respectively. The results in Fig. 4 demonstrate that the squared magnitude of $T^{JL}_{\rm DWBA}$ for the lower JL are

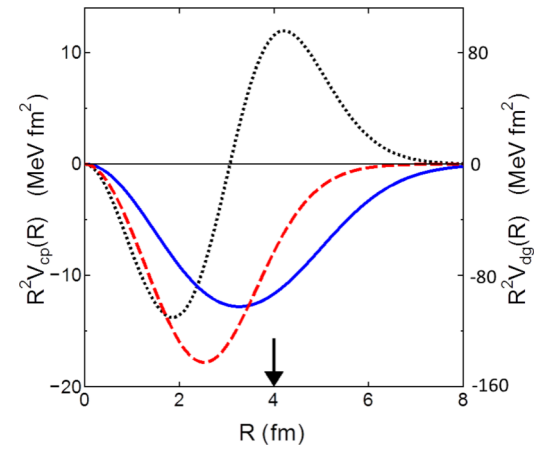

FIG. 5. (Color online) Radial shape of the coupling [$V_{\rm cp}(R)$] and diagonal [$V_{\rm dg}(R)$] potentials. The diagonal potential multiplied by R^2 for the elastic 0_1^+ channel is shown by the dashed curve, while that for the inelastic 0_2^+ channel is shown by the thick solid curve. The coupling potential of $0_1^+ \to 0_2^+$ is shown by the dotted curve. The right-side ordinate corresponds to the strength of the diagonal potentials, while the coupling potential is plotted with the left-side ordinate. The magnitude of both diagonal potentials are multiplied by the factor 1/8. The arrow at $R = 4$ fm shows the distance, at which the absorption effect becomes strong. See text for details.

TABLE II. Effective orbital spin $\bar{L}$ with measure (I) and scattering radius $R_{\rm SC}$ for the 0_2^+ channel. In the top row, the results of the full MCC calculation are shown, while the results without the distortion potential in the exit 0_2^+ channel are shown at the bottom row. See text for details.

Channel	$\bar{L}$	$R_{\rm SC}$ (fm)	$\bar{r}$ (fm)
0_2^+ (Full calculation)	6.13	3.46	3.47
0_2^+ (No distortion potential)	5.46	3.09	3.47

prominently reduced if the distortion potential in the final 0_2^+ channel is switched on.

The radial distribution of $V_{\rm cp}$ (dotted curve) has negative and positive peaks at $r \sim 2$ fm and $r \sim 4$ fm, respectively. The transition to the 0_2^+ state mainly occurs around these two distances. The diagonal potential in the final 0_2^+ channel (thick curve) is longer range than the range of the elastic potential (dashed curve), and the attraction of the final 0_2^+ channel covers the entire range of the coupling potential. Therefore, the final distorted wave $\chi^{JL}_{0_2^+}$ is trapped around the peak positions of the coupling potential when the absorptive potential is switched off. Because there is strong absorption at the inner region of $r \leqslant 4$ fm, shown by the arrow (see also the solid squares in Fig. 1), the amplitude of $\chi^{JL}_{0_2^+}$ trapped at $r \sim 2$ fm is strongly absorbed. This inner absorption for the final distorted wave leads to reduction of the product of $V_{\rm cp}\chi^{JL}_{0_2^+}$; hence, the magnitude of $T^{JL}_{\rm DWBA}$. The absorption of the inner distorted wave is strongly masked for the higher JL because of the large effect of the centrifugal potential. Therefore, a strong reduction in the partial cross section arises in the lower JL region, but the distribution is almost unchanged in the higher JL.

The $\bar{L}$ and $R_{\rm SC}$ obtained with and without the distortion potential in the exit 3α channel are summarized in Table II. Here we use measure (I) in calculating $\bar{L}$ and $R_{\rm SC}$. The $R_{\rm SC}$ without the distortion is 3.09 fm, which is smaller by about 10% than the result of the full MCC calculation, $R_{\rm SC} = 3.46$ fm. Although the distortion effect in the exit channel changes the distribution of the partial cross section considerably, the distortion effect can be negligible in determining the magnitude of the scattering radius. Therefore, we can conclude that the main factor in determining the scattering radius is not the distortion potential in the exit 0_2^+ channel, but the coupling potential for the transition of $0_1^+ \to 0_2^+$. The enhancement of the scattering radius in the 0_2^+ channel is mainly attributable to the spatial extension of the coupling potential. These results are completely consistent with the analysis by Takashina *et al.* [17,18].

IV. 3α CLUSTER EXCITATION VERSUS GMR EXCITATION

A strong enhancement has been clearly observed in the scattering radius of the 3α exit channel. The scattering radius for the inelastic scattering basically reflects the spatial range of the transition potential for $0_1^+ \to 0_2^+$. In this section, we discuss whether the enhanced scattering radius is a peculiar phenomenon in the 3α excitation, which involves a spatially extended structure, or not. To investigate the peculiarity of the 3α excitation, we should introduce a completely different type of the monopole 0^+ excitation and compare it with the 3α monopole excitation. A cluster excitation should be compared with a collective motion generated by coherent excitations of nucleons moving in a uniform mean field, for example.

In a mean-field picture, a monopole excitation of $0_1^+ \to 0_2^+$ is induced by a monopole compression mode, which is a small spherical oscillation of a nuclear surface [19]. Experimentally, such a monopole compression mode has been observed as a GMR. In the following analysis, we assume an isolated monopole compression mode located at the empirical excitation energy of GMR, and the scattering radius for the inelastic scattering going to GMR (0_2^+) is calculated.

According to systematic experimental studies, an empirical excitation energy of GMR for a mass number A is known to be

$$E_x^{\rm GMR} \sim 80A^{-1/3}({\rm MeV}). \tag{21}$$

In the case of ^{12}C, $E_x^{\rm GMR}$ becomes about 35 MeV. As for the transition density to the GMR state (0_2^+), the so-called Bohr-Mottleson (BM) model [31],

$$\rho^{\rm BM}_{0_1^+\to 0_2^+}(r) = -\beta\left[3\rho_{0_1^+}(r) + r\frac{d\rho_{0_1^+}(r)}{dr}\right], \tag{22}$$

is usually employed in analysis of the hadronic excitation of GMR [32,33]. According to Eq. (22), we can obtain the transition density for the GMR excitation in a quite simple manner, but several RPA calculations have resulted in transition densities that are very similar to this BM form in the heavier mass region [34]. In this model, the density distribution of the excited GMR state (0_2^+) is simply obtained as

$$\rho^{\rm BM}_{0_2^+}(r) = \rho_{0_1^+}(r) + \rho^{\rm BM}_{0_1^+\to 0_2^+}(r). \tag{23}$$

The mean radius calculated from the density in Eq. (23) is $\bar{r} = 2.62$ fm. The strength β is generally determined so as to reproduce the magnitude of the experimental cross section of GMR. In the present analysis, the transition strength β is fixed so as to reproduce the magnitude of the isoscalar monopole matrix element for the 3α excitation, which is given by

$$M(IS,0_1^+ \to 0_2^+) = \int_0^\infty \rho^{3\alpha}_{0_1^+\to 0_2^+}(r)r^2 d\mathbf{r}. \tag{24}$$

Here $\rho^{3\alpha}_{0_1^+\to 0_2^+}(r)$ is a transition density calculated from the 3α RGM [2]. We found that $\beta = 0.09$ can reproduce $M(IS,0_1^+ \to 0_2^+)$ in Eq. (24). However, $\beta = 0.09$ is much stronger than a realistic strength for the GMR excitation. In the 3α RGM, the monopole strength going to the 0_2^+ state at $E_x = 7.65$ MeV exhausts about 23% of the energy-weighted sum rule (EWSR). If we directly use the monopole strength obtained by Eq. (24) for GMR assumed at $E_x^{\rm GMR} = 35$ MeV, this GMR completely exhausts the EWSR value (∼100%); hence, the assumed strength, $\beta = 0.09$, is too strong. According to the analysis of the α scattering by ^{58}Ni [33], the EWSR fraction for GMR is about 20%–30%. Therefore, a realistic strength β may be reduced to about half of the strength fixed here.

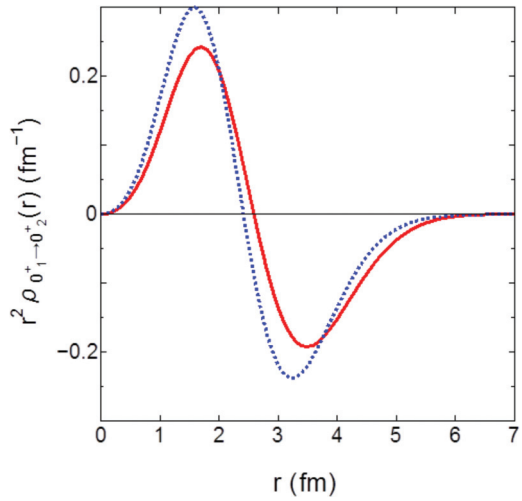

FIG. 6. (Color online) Radial part of the transition density for $0_1^+ \to 0_2^+$. The squared radius r^2 is multiplied to the transition density. The solid curve shows the density calculated by the microscopic 3α cluster model, while the dotted curve represents the density obtained by the BM model. The BM density is multiplied by a minus sign.

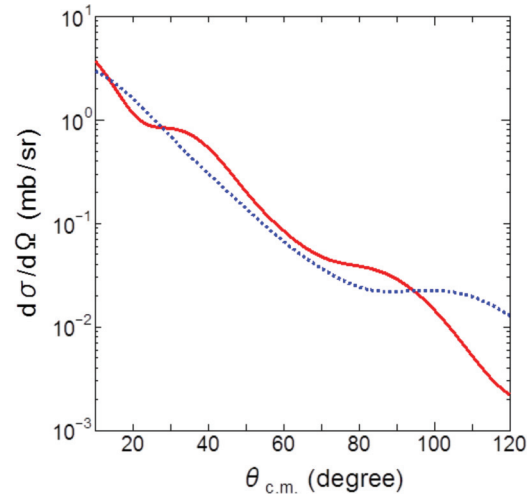

FIG. 7. (Color online) Comparison of differential cross sections for inelastic scattering at $E_p = 65$ MeV. The solid and dotted curves represent the calculation based on the cluster and BM transition densities, respectively.

The radial part of the transition densities, $\rho_{0_1^+ \to 0_2^+}(r)$, obtained by the 3α cluster model and the BM model are shown in Fig. 6. Here the radial part of the transition density is defined by $\rho_{0_1^+ \to 0_2^+}(\mathbf{r}) = \rho_{0_1^+ \to 0_2^+}(r) Y_{00}(\hat{\mathbf{r}})$ with a spherical harmonics of $Y_{00}(\hat{\mathbf{r}})$. The radial behaviors are quite similar to each other, and both densities have one node around $r \sim 2.8$ fm. This behavior is attributable to the conservation condition on the nucleon number. Although the transition density in the 3α cluster model (solid curve) has a slightly extended distribution in comparison to the BM density (dotted curve), the difference in the range is not so large (about 0.5 fm). The transition potentials calculated by the folding procedure in Eqs. (13) and (15) also reveal similar behavior in these two model because of the similarity of the transition density.

We assume an isolated GMR at $E_x^{\text{GMR}} = 35$ MeV with the densities given by Eqs. (22) and (23), and the MCC calculation for the GMR excitation by the proton scattering at $E_p = 65$ MeV is performed. In the MCC calculation for GMR, the phenomenological complex potentials, optimized to reproduce the experiments of the cluster excitations, is unchanged for simplicity. The differential cross section for the GMR excitation is shown in Fig. 7. In this figure, the dotted curve shows the differential cross section going to the GMR state, while the solid curve represents the excitation to the 3α cluster state. In the backward region, the cross section for the GMR excitation has a large yield; hence, the angular distribution for the GMR excitation shows more isotropic behavior than the distribution for the 3α excitation.

The differences observed in the differential cross section suggest that the distribution of the partial cross section is very different in these two excitation schemes, the 3α and GMR excitations. The partial cross sections for the inelastic scattering are shown in Fig. 8. We can clearly confirm a different distribution in these two excitation models. The partial cross section for the GMR excitation (squares) is rapidly damped around $J = 15/2$, while the result for the cluster excitation (stars) has an extended structure ranging up to $J = 19/2$. This difference in the distribution can be naturally understood from the angular distribution shown in Fig. 7. The differential cross section for GMR increases at a backward angle. This means the fluctuation of the scattering angle ($\Delta\theta$) becomes large in the GMR excitation. Therefore, the fluctuation of the scattered angular momentum (ΔL) for the GMR excitation is reduced more than ΔL (and ΔJ) for the 3α excitation according to the uncertainty relation of $\Delta L \Delta\theta \sim \hbar$.

The obtained $\bar{L}$ and R_{SC} in the elastic, 3α inelastic and GMR inelastic scattering are summarized in Table III. In accordance with the reduction of ΔL in GMR, the effective orbital spin $\bar{L}$ and the scattering radius R_{SC} are reduced to $\bar{L} = 4.09$ and $R_{\text{SC}} = 2.31$ fm for GMR. The scattering radius for GMR is almost the same as its matter radius of $\bar{r} = 2.62$ fm. These values are considerably smaller than the results obtained by the 3α excitation, $R_{\text{SC}} = 3.46$ fm and $\bar{L} = 6.13$. As shown in Fig. 6, the transition densities for the GMR and 3α excitations reveal almost the same behavior. Thus, the main origin of the

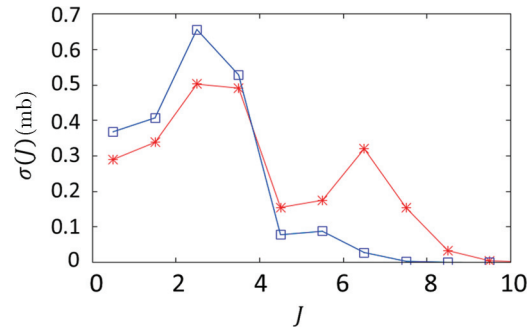

FIG. 8. (Color online) Distributions of the partial cross section in the inelastic scattering at $E_p = 65$ MeV. The asterisks show the distribution for the 3α cluster state, 0_2^+, while the squares show that for the GMR state.

TABLE III. Effective orbital spin $\bar{L}$ and scattering radius R_{SC} calculated from the definition in Eq. (1). At the rightmost column, the mean matter radii are presented for comparison. See text for details.

State	Energy (MeV)	$\bar{L}$	R_{SC} (fm)	$\bar{r}$ (fm)
0_1^+ (Elastic)	0.00	4.69	2.65	2.40
0_2^+ (3α)	7.65	6.13	3.46	3.47
0_2^+ (GMR)	35.0	4.09	2.31	2.62

difference in R_{SC} between the 3α excitation (3.47 fm) and the GMR excitation (2.31 fm) is not a difference of the radial shape of the transition density. The difference in R_{SC} is attributed to the difference of the excitation energies between the 3α state (7.65 MeV) and the GMR state (35.0 MeV). In a high-energy scattering theory, such as Blair's phase rule [15], the internal excitation energy of colliding nuclei is usually neglected, but the difference in the excitation energy plays an important role in determining the scattering radius. Specifically, there is a Q-value effect on the magnitude of the scattering radius.

To investigate the Q-value effect for the monopole transition from 0_1^+ to 0_2^+ more clearly, we artificially vary the excitation energy of the 0_2^+ state in the range of $E_x = 0 - 45$ MeV, and the coupled-channels for $p + {}^{12}\mathrm{C}_{\mathrm{g.s.}} \rightarrow p + {}^{12}\mathrm{C}(0_2^+)$ are solved for the individual excitation energies of the 0_2^+ state. In this calculation, the transition density obtained by the 3α RGM is used for the monopole excitation. The excitation energy dependence of R_{SC} is shown in Fig. 9. The curve with the solid squares is the result of the scattering radius at the proton's incident energy of $E_p = 65$ MeV, while the curve with the crosses show the same result at $E_p = 200$ MeV.

In the case of $E_p = 65$ MeV, R_{SC} for the 0_2^+ state reaches a maximum value of about 3.6 fm at the zero excitation energy

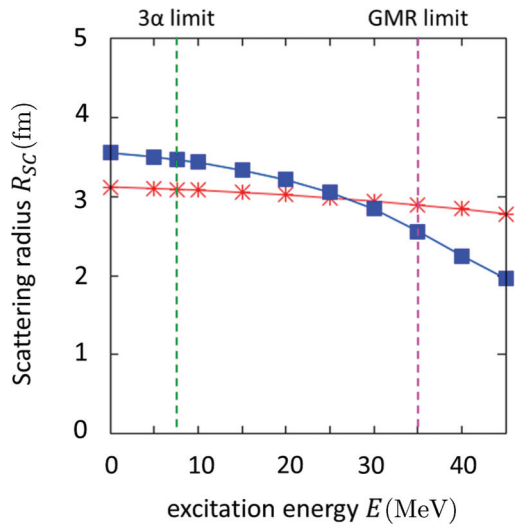

FIG. 9. (Color online) Excitation energy dependence of scattering radius. The abscissa represents the excitation energy, while the ordinate represents the scattering radius R_{SC}. The solid squares and crosses denote the R_{SC} calculated for $E_p = 65$ and 200 MeV, respectively. The dotted line at $E_x = 7.65$ MeV represents the excitation energy of the 3α cluster excitation, while the line at $E_x = 35$ MeV shows the energy of the GMR excitation.

limit. However, R_{SC} monotonically decreases as the excitation energy is taken to be higher. The R_{SC} at the 3α limit at $E_x = 7.65$ MeV is almost the same as the maximum value at $E_x = 0$ MeV, while R_{SC} at the GMR limit at $E_x = 35$ MeV is strongly reduced. Therefore, the Q-value effect as well as the radial shape of the coupling potential plays an essential role in the determination of the scattering radius, which characterizes the spatial size of the reaction area. However, this Q-value effect becomes weak in the scattering at $E_p = 200$ MeV. As shown by the crosses, R_{SC} reveals an almost constant behavior with respect to the variation of the excitation energy. If the proton incident energy becomes quite high, the difference of the excitation energy can be negligible in determining the scattering radius. The resultant R_{SC} at $E_p = 200$ MeV is about 3.2 fm at the 3α excitation energy, which is the same value as the radius obtained by the diffraction model [11].

V. ENERGY SYSTEMATICS OF THE SCATTERING RADIUS

We extend the analysis of the scattering radius at $E_p = 65$ MeV to other incident energy, $E_p = 29.95, 35.2, 39.95$, and 200 MeV. In the calculation of 65 MeV, a fit to the experimental data of the 0_2^+ channel is not so good if N_R is set close to 1. Furthermore, in the lower-energy region of $E_p = 29.95, 35.2, 39.95$ MeV, the reproduction of the experimental data becomes more difficult in the calculation of $N_R \sim 1$. Therefore, in the whole energy region, we search possible parameter sets, which reasonably reproduce the observed angular distributions, by varying N_R in the range of $N_R^{\mathrm{CE}} = 0.7$–1.5 for the central part and $N_R^{\mathrm{LS}} = 0.6$–3.0 for the spin-orbit part. For all the obtained parameter sets, we derive the effective orbital spin $\bar{L}$ and the scattering radius R_{SC}. To clarify the ambiguity of R_{SC}, which originates from the variation of the employed parameter sets, we average all the scattering radii obtained for the different parameter sets at a fixed energy.

Energy systematics of the averaged R_{SC} are shown in Fig. 10. The solid circles and solid squares show the R_{SC} of the elastic and inelastic channels, respectively. The ambiguity of R_{SC} at a fixed energy is determined by the standard deviation of an obtained set of R_{SC}, which is shown by the error bar attached to the circles and the squares. R_{SC} contains the ambiguity of about 11% at a maximum (3α channel at $E_p = 35.2$ MeV). In the low-energy region of $E_p \leqslant 40$ MeV, R_{SC} reveals energy-dependent behavior with a considerable ambiguity, while the energy dependence seems to be weak in the high-energy region of $E_p \geqslant 65$ MeV, although data points do not exist between 65 and 200 MeV.

The white circle and white square represent the diffraction radii obtained from elastic and inelastic scattering at $E_p = 1040$ MeV, respectively [11]. The magnitude of the scattering radii at $E_p = 200$ MeV is consistent with the magnitude of the diffraction radii. The scattering radius for the 3α excitation is systematically larger than that for the elastic scattering. This means that the scattering radius can be treated as a characteristic size for a nucleus. The values of the scattering radius for the elastic and 0_2^+ channels distribute around the respective matter radius, shown by the dotted lines, although the scattering radius does not necessarily represent the matter radius itself.

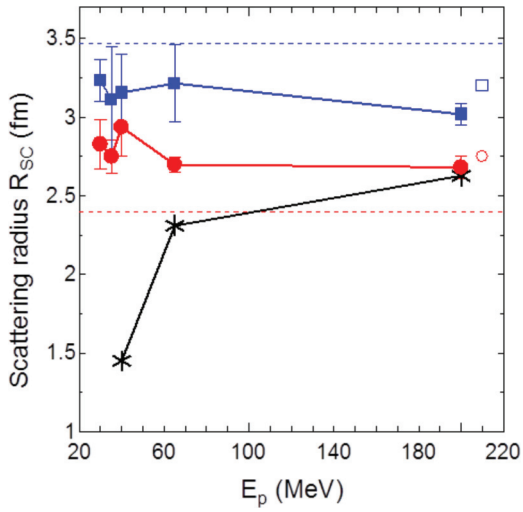

FIG. 10. (Color online) Energy dependence of scattering radius R_{SC}. The solid squares show R_{SC} for the 3α excitation, while the solid circles show the radius for the elastic scattering. The asterisks represent R_{SC} for GMR excitation. The upper and lower dotted lines show the matter radius of the 0_2^+ and 0_1^+ states, respectively. The white symbols are the diffraction radii derived from proton scattering at $E_p = 1040$ MeV [11]. See text for details.

The scattering radius for the GMR excitation is shown by the asterisk. The GMR scattering radius is smaller than the 3α scattering radius, and it shows a strong energy dependence. At $E_p = 29.95$ and 35.2 MeV, there is no plot of R_{SC}. In these energies, the GMR channel is closed because the proton's incident energy in the center-of-mass system is lower than the GMR excitation energy. In such a low incident energy, no partial waves are scattered to the GMR state; hence, the calculation of R_{SC} is meaningless. If the incident energy is just above the GMR excitation energy, the range of the scattered partial waves is sensitive to the variation of the incident energy. Thus, R_{SC} has an energy dependence around the incident energy just above the threshold of GMR, for example, $E_p \leqslant 50$ MeV.

VI. SUMMARY AND DISCUSSION

In this paper, we have introduced the scattering radius on the basis of the partial-wave expansion method, which is a standard technique in a scattering problem. The scattering radius is defined by the partial cross section. In the high-energy limit of an elastic scattering by a black sphere, we have found a clear relation of the scattering radius and the matter radius. Therefore, the scattering radius introduced in the present study characterizes the radius of a spatial region, where a scattering or an exclusive reaction occurs. The MCC calculation has been performed for the $p + {}^{12}$C scattering at $E_p = 29.95$–200 MeV, and the differential cross sections for both the elastic and the inelastic scattering are reasonably reproduced.

From the partial-wave analysis of the MCC calculation, the scattering radii are evaluated for individual exit channels: the elastic channel and the 0_2^+ channel with a well-developed 3α structure. We have introduced two kinds of scattering radius, which depend on the moment of the orbital spin. In the elastic scattering, the scattering radius, calculated from the fourth and second moments of the orbital spin, is considerably larger than the radius of the matter density in the ground state; hence, the scattering radius with the four and second moments is employed as a measure of the scattering area. We have found a clear enhancement of the scattering radius for the inelastic scattering going to the Hoyle 0_2^+ state. Because the distortion potential in the exit 0_2^+ channel plays a minor role, the scattering radius for the inelastic scattering mainly provides information on the spatial size of the transition potential for ${}^{12}\mathrm{C}_{\mathrm{g.s.}} \rightarrow {}^{12}\mathrm{C}(0_2^+)$. This result is consistent with Takashina's pioneering works [17,18].

We have also assumed the existence of an isolated GMR at $E_x = 35$ MeV, and the differential cross section of the monopole transition of ${}^{12}\mathrm{C}_{\mathrm{g.s.}} \rightarrow {}^{12}\mathrm{C}(\mathrm{GMR})$ has been calculated. The angular range of the differential cross section for the GMR excitation is extended to the backward angle. This extension of angular distribution leads to a reduction of the distribution width in the partial cross sections. Because the distribution of the partial cross section is more localized within a small range of the angular momentum, the R_{SC} for GMR is prominently reduced in comparison to the result of the 3α cluster excitation. The difference in the scattering radius between the 3α excitation and the GMR excitation is attributable to the large difference of their excitation energy because no prominent difference can be seen in the shape of the transition densities for these two transitions. Thus, the difference in the scattering radius arises from the Q-value effect of reactions.

The Q-value effect on the scattering radius can be summarized as follows. After an incident proton hits the ^{12}C nucleus, ^{12}C is excited to the 3α state or GMR. In the case of the 3α excitation, the excitation energy is low; hence, the scattered proton can carry the higher partial-wave components, which have a good overlap with the transition potential at a large distance. The components of the higher partial waves lead to the enhancement of the scattering radius. On the contrary, the incident proton largely loses incident energy in the GMR excitation. In such a situation, the proton cannot penetrate the effective barrier for the higher partial waves, and only the lower partial waves can contribute to the scattering process. This is the main reason why the partial cross section is limited to the lower partial-wave components in the GMR excitation. This Q-value effect becomes weak in the limit of the high-energy scattering, but a considerable difference of the scattering radius still can be seen at $E_p = 200$ MeV between the 3α excitation and the GMR excitation.

Although the spatial shape of the transition density or the coupling potential is a main ingredient for the enhanced scattering radius in the 3α excitation, the small excitation energy of the 3α state is also an important factor for the enhancement of the scattering radius. The low energy of the cluster monopole excitation is an anomalous feature, which can never be seen in a uniform mean-field picture. Because an incompressibility of nuclear matter is quite high, about 200 MeV, large excitation energy is always required to produce the monopole compression mode of a nuclear surface. That is, the compression mode has quite a high frequency. In marked contrast to this high-frequency mode, the excitation

energy of cluster states is quite small, and clusters are weakly coupled to each other because cluster states appear around the threshold energy for decay into corresponding subunits. This weak-coupling feature leads to the formation of the clusters' monopole oscillation with much a smaller frequency than the uniform compression mode. This small frequency of the cluster monopole oscillation indeed causes the enhancement of the scattering radius in the excitation going to the cluster state.

In the present study, we restricted the MCC calculation to the two-channel problem, including only the incident and exit channels, to investigate the essential features of the scattering radius. Although the essential dynamics for the elastic and inelastic scattering to the 0_2^+ state can be covered in the two-channel calculation, the scattering radius for the other inelastic channels, such as the rotational 2_1^+ excitation and the vibrational 3_1^- excitation, should be analyzed in the same MCC framework. In addition, the reproduction of the experimental cross section is not so successful in the present MCC calculation. We have tried to reproduce the observed cross section by varying the strength of the folding potential, but the precise reproduction has not been obtained. Of course, the qualitative features of the scattering radius are not expected to be particularly sensitive to a detailed structure of the calculated angular distribution, but the MCC calculation should be revised to obtain better fitting data.

For future study, therefore, we perform a more realistic MCC calculation, in which the low-lying collective 2_1^+, 3_1^- states and the 2_2^+ state, which correspond to the rotational excitation of the Hoyle 0_2^+ state, are explicitly coupled. To improve the reproduction of the scattering observables, the density-dependent nucleon-nucleon interaction should be employed. By performing the revised MCC calculation, the scattering radius should be discussed in other collective excitation channels. The improved MCC calculation will be reported in forthcoming papers.

Finally, we need to comment on the definitions of an effective orbital spin. In the present study, we have assumed simple definitions to extract a representative value of orbital spins from a set of the partial cross sections, but the present assumptions are not completed, and there could be other possible variations in defining an effective orbital spin. Therefore, establishing an empirical rule for an effective orbital spin from systematic studies is important. In particular, the relation between matter radii and the scattering cross sections has been extensively discussed in high-energy elastic scattering [10]. Therefore, an analysis of the scattering radius should be applied to a wide range of elastic scattering. Systematic studies of elastic scattering are now under way.

ACKNOWLEDGMENTS

The authors would like to thank Professor A. Kohama and P. Schuck for their careful reading of the manuscript and their encouragements. We also thank Professor Y. Iseri for his tutorial support of the computational program. One of the authors (M.I.) also thanks Dr. K. Minomo for his valuable comments and R. Nishioka for providing the information on his numerical calculation of the neutron-nucleus scattering.

TABLE IV. The parameter set of the absorptive potentials for the elastic channel. The diffuseness parameters are taken to be a constant of $a_{IV} = a_{IS} = 0.6$ fm except for the surface potential at $E_p = 200$ MeV ($a_{IS} = 0.8$ fm). The leftmost column show the proton's incident energy. W_{0V} and R_{IV} show the strength and radius parameters for the volume type potential, respectively, while W_{0S} and R_{IS} show the respective parameters for the surface type potential. Incident energy and W_0 are shown in units of MeV, while R_I is shown in units of fm.

Energy	W_{0V}	R_{IV}	W_{0S}	R_{IS}
29.95	6.5	3.0	2.0	2.0
35.2	6.2	3.0	3.6	2.0
39.95	6.0	3.0	5.0	2.0
65.0	5.0	2.8	10.0	2.5
200.0	25.0	2.5	23.0	2.5

APPENDIX

In this Appendix, we show the parameter set of the phenomenological complex potentials, which are introduced in the diagonal transition in the coupling potentials. In the following parameter sets, the strength of the folding potentials are fixed at $N_R^{\mathrm{CE}} = 1$ (central part) and $N_R^{\mathrm{LS}} = 1.1$ (spin-orbit part). In Table IV, the parameter set for the elastic channel is shown. The employed imaginary potentials have the form factors of the volume (V) and surface (S) WSs. Each potential contains the parameters of the depth (W_0) and the radius (R_I), which are distinguished by the subscripts of V and S for the volume and surface parts, respectively. The diffuseness parameters are commonly fixed to 0.6 fm except for the energy of $E_p = 200$ MeV. At $E_p = 200$ MeV, the diffuseness of the surface potential is extended to $a_{IS} = 0.8$ fm.

In Table V, the parameters introduced in the inelastic channels are shown. In addition to the volume + surface imaginary potentials, we introduced the surface-type real potential to simulate a dynamic polarization effect originates from the excitation to the 2_2^+ state, which is the 3α rotational excited state of the 0_2^+ state. The depth and radius of the real potential are shown by V_{0S} and R_S, respectively. In the inelastic channel, all the diffuseness parameters are set to 0.6 fm.

TABLE V. The same as Table IV, but for the exit 0_2^+ channel. The diffuseness parameters are set to $a_{IV} = a_{IS} = a_S = 0.6$ fm. V_{0S} and R_S are the parameters for a real potential with a surface WS form factor.

Energy	W_{0V}	R_{IV}	W_{0S}	R_{IS}	V_{0S}	R_S
29.95	3.0	2.0	5.0	3.5	9.0	4.2
35.2	3.0	2.4	5.5	3.0	8.5	4.2
39.95	3.0	2.8	6.0	2.8	8.0	4.2
65.0	3.0	5.0	9.0	2.4	6.0	4.2
200.0	8.0	5.0	6.0	4.0	0.0	4.2

[1] K. Ikeda *et al*., Prog. Theor. Phys. **68**, 1 (1980), and references therein.

[2] Y. Fukushima and M. Kamimura, J. Phys. Soc. Jpn. **44**, 225 (1977); M. Kamimura, Nucl. Phys. A **351**, 456 (1981).

[3] E. Uegaki, S. Okabe, Y. Abe, and M. Tanaka, Prog. Theor. Phys. **57**, 1262 (1977); **62**, 1621 (1979).

[4] A. Tohsaki, H. Horiuchi, P. Schuck, and G. Röpke, Phys. Rev. Lett. **87**, 192501 (2001).

[5] Y. Funaki, A. Tohsaki, H. Horiuchi, P. Schuck, and G. Röpke, Phys. Rev. C **67**, 051306(R) (2003), and references therein.

[6] Y. Suzuki, Prog. Theor. Phys. **55**, 1751 (1976); **56**, 111 (1976).

[7] T. Matsuse, M. Kamimura, and Y. Fukushima, Prog. Theor. Phys. **53**, 706 (1975).

[8] K. Ikeda, N. Takigawa, and H. Horiuchi, Prog. Theor. Phys. Suppl. **E68**, 464 (1968).

[9] A. N. Danilov, T. L. Belyaeva, A. S. Demyanova, S. A. Goncharov, and A. A. Ogloblin, Phys. Rev. C **80**, 054603 (2009).

[10] A. Kohama, K. Iida, and K. Oyamatsu, Phys. Rev. C **69**, 064316 (2004).

[11] K. Iida, S. Koide, A. Kohama, and K. Oyamatsu, Mod. Phys. Lett. A **27**, 1250020 (2012).

[12] S. Ohkubo and Y. Hirabayashi, Phys. Rev. C **70**, 041602(R) (2004).

[13] S. Ohkubo and Y. Hirabayashi, Phys. Rev. C **75**, 044609 (2007).

[14] Sh. Hamada, Y. Hirabayashi, N. Burtebayev, and S. Ohkubo, Phys. Rev. C **87**, 024311 (2013).

[15] J. S. Blair, Phys. Rev. **115**, 928 (1959).

[16] M. Ito, Y. Hirabayashi, and Y. Sakuragi, Phys. Rev. C **66**, 034307 (2002); M. Ito, Y. Sakuragi, and Y. Hirabayashi, *ibid*. **63**, 064303 (2001), and references therein.

[17] M. Takashina and Y. Sakuragi, Phys. Rev. C **74**, 054606 (2006).

[18] M. Takashina, Phys. Rev. C **78**, 014602 (2008).

[19] P. Ring and P. Schuck, *Nuclear Many-Body Problem*, 1st ed. (Springer Verlag, Berlin, Heidelberg, New York, 2004).

[20] S. Hashimoto, M. Yahiro, K. Ogata, K. Minomo, and S. Chiba, Phys. Rev. C **83**, 054617 (2011).

[21] G. R. Satchler and W. G. Love, Phys. Rep. **55**, 183 (1979).

[22] G. Bertsch, J. Borysowicz, H. Macmanus, and W. G. Love, Nucl. Phys. A **284**, 399 (1977).

[23] F. A. Brieva and J. R. Rook, Nucl. Phys. A **291**, 206 (1978).

[24] A. M. Kobos, B. A. Brown, P. E. Hodgson, G. R. Satchler, and A. Budzanowski, Nucl. Phys. A **384**, 65 (1982).

[25] D. T. Khoa, G. R. Satchler, and W. von Oertzen, Phys. Rev. C **56**, 954 (1997).

[26] K. Amos, P. J. Dortmans, H. V. von Geramb, S. Karataglidits, and J. Raynal, in *Advances in Nuclear Physics*, edited by J. W. Negel and E. Vogt (Plenum, New York, 2000), Vol. 25, p. 275.

[27] T. Furumoto and Y. Sakuragi, Phys. Rev. C **78**, 044610 (2008); **79**, 011601(R) (2009); **80**, 044614 (2009).

[28] Y. Sakuragi, M. Yahiro, and M. Kamimura, Prog. Theor. Phys. Suppl. **89**, 136 (1989).

[29] M. Ito, Y. Sakuragi, and Y. Hirabayashi, Eur. Phys. J. A **5**, 373 (1999).

[30] D. T. Khoa and D. C. Cuong, Phys. Lett. B **660**, 331 (2008).

[31] A. Bohr and B. R. Mottelson, *Nuclear Structure* (Benjamin, New York, 1975), Vol. 2.

[32] D. J. Horen, J. R. Beene, and G. R. Satchler, Phys. Rev. C **52**, 1554 (1995).

[33] G. R. Satchler and Dao T. Khoa, Phys. Rev. C **55**, 285 (1997).

[34] J. P. Blaizot, Phys. Rep. **64**, 171 (1980).